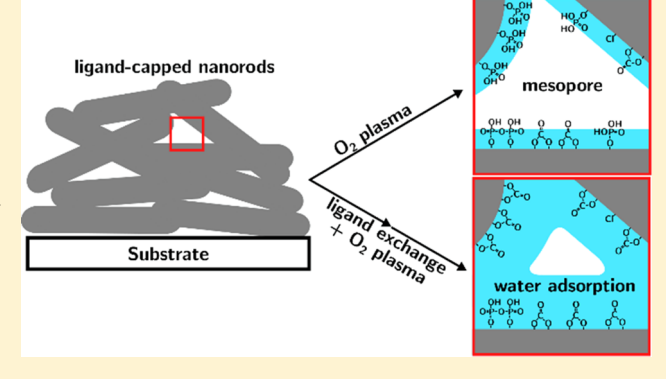
THE JOURNAL OF PHYSICAL CHEMISTRY

Self-Regulated Porosity and Reactivity in Mesoporous **Heterogeneous Catalysts Using Colloidal Nanocrystals**

Xinchun Tian, [†] Tian Wei Goh, ^{‡,} ○ Oliver VandenBerg, § Jeremy VanDerslice, ^{||} Tiago Fiorini da Silva, [±] Fabian Naab, [#] Jennifer L. Hay, ¶ Julia J. Chang, † Bin Yuan, †, ∇ Frank C. Peiris, § Wenyu Huang, †, ○ and Ludovico Cademartiri*, †, ∇, ○ and Ludovico Cademartiriii Cademartiriii Cademartiriii Cademartiriii Cademartiriii Cademartiriii Cademartiriii Cademartiriii Cademartiriii Cademartiriiii Cademartiriii Cademartiriii Cademartiriii Cademartiriii Cadema

Supporting Information

ABSTRACT: This paper describes the creation of mesoporous inorganic films based on the plasma processing of ligandcapped nanocrystals. We use nanorods of HfO2 as a model system and report an extensive characterization of the chemistry, structure, mechanical properties, and reactivity to show that (i) the aspect ratio of the nanorods regulates the pore size and pore volume of the films in a predictable manner and yields an increase in porosity over spherical nanocrystals of up to 60%, (ii) the modulus (>25 GPa) and hardness (>1.1 GPa) are sufficient to tolerate chemical-mechanical planarization, and (iii) the catalytic activity can be finely controlled by the choice of ligands, which regulate the surface chemistry and water adsorption in the final product. This approach is an attractive route to create—in two simple and scalable steps—



crack-free inorganic mesoporous films for applications in catalysis, energy storage, energy harvesting, and more.

■ INTRODUCTION

Colloidal nanocrystals (CNs) are attractive building blocks for the creation of mesoporous thin films¹⁻⁴ or clusters⁵⁻⁹ because of the control over their size, shape, composition, and surface chemistry. 10,11 Their assembly into mesoporous films with large, accessible pores requires the use of a porogen and its later removal after assembly, which is significantly challenging (e.g., incomplete removal, pore collapse, cracking). 1-3

Therefore, there is a continuous interest in consolidating CNs to make mesoporous materials without the use of porogens for catalysts, annocomposite electrochromic films, a drug delivery,⁶ bioseparation,⁷ sensing,⁸ and more. However, the characterization of the pore space in these systems is complicated by their small volume, 12 the residual organics 12 and water 13 in their pores, and the structural defects caused by

ligand removal (cracks, pinholes, etc.). 14 Therefore, the understanding of how particle size, shape, capping ligands, and postprocessing affect the key functionalities of these systems (pore structure, surface chemistry, and mechanical properties) is very limited.

Over the past few years, we have demonstrated that nonthermal plasma processing allows to convert spin-coated assemblies of ligand-capped spherical nanocrystals into allinorganic, crack-free films, whose nanostructure preserves the crystal size and shape of the original building blocks and whose mechanical properties are comparable to those of the sintered

Received: April 20, 2019 Revised: June 28, 2019 Published: July 11, 2019



[†]Department of Materials Science & Engineering, Iowa State University of Science and Technology, Hoover Hall, Ames 50011, Iowa, United States

^{*}Department of Chemistry, Iowa State University of Science and Technology, Gilman Hall, Ames 50011, Iowa, United States

[§]Department of Physics, Kenyon College, Gambier 43022, Ohio, United States

I. A. Woollam Company, Lincoln 68508, Nebraska, United States

¹Department of Nuclear Physics, Institute of Physics of University of São Paulo, São Paulo 05315-970, Brazil

^{*}Michigan Ion Beam Laboratory, University of Michigan, Draper Road, Ann Arbor, Michigan 48109, United States

[¶]KLA-Tencor, 105 Meco Lane, Oak Ridge, Tennessee 37830, United States

 $^{^{}m V}$ Department of Chemical & Biological Engineering, Iowa State University of Science and Technology, Sweeney Hall, Ames 50011, Iowa, United States

OAmes Laboratory, U.S. Department of Energy, Ames 50011, Iowa, United States

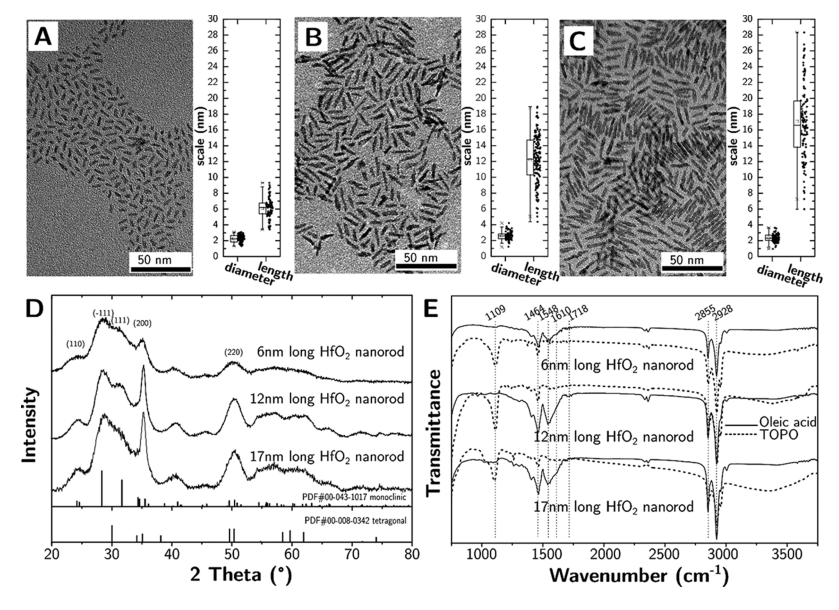


Figure 1. Nanocrystals as building blocks. (A–C) OA-capped HfO₂ (OA-HfO₂ for short) nanocrystals with different ARs. (D) XRD patterns of the three types of nanocrystals. (E) FT-IR spectra of the three types of nanocrystals, wherein ligand exchange was used to replace originally capped TOPO with OA.

analogue. ^{12–17} Plasma processing fully removes the ligands by the combined action of radicals and UV radiation ¹⁶ and causes the opening of the interstitial pores ¹⁷ (up to the expected random close-packed pore volume of 32%), followed by their spontaneous filling with strongly bound adventitious water. ¹³ We believe that the strong adsorption of water in the pores is a result of the exposure of the bare, high energy surfaces of the nanocrystals and is consistent with their remarkably high mechanical properties. ^{17,18}

Although the porosity observed in our films obtained from spherical nanoparticles was encouraging, it was insufficient in magnitude (\sim 32%) to truly qualify the material as mesoporous and it was completely occluded by water because of the small pore size and high surface energies.

In this article, we show that the aspect ratio (AR) of HfO₂ nanorod building blocks allows for the deliberate increase of porosity (up to 55% pore volume) and pore size and the opening up of the pores to relatively large molecules (141.9 m²/cm³ or 33.7 m²/g of surface area accessible to toluene at room temperature). Characterization of the toluene adsorption isotherms by ellipsometric porosimetry (EP) shows hysteresis of type H2(a), which are characteristic of mesopores with necks in the pore network. Increasing the AR of the nanoparticles and therefore the porosity of the films does not compromise their crack-free nature and predictably reduces their mechanical strength but not enough to preclude them from chemical-mechanical planarization (CMP). Last, we show that the chemical reactivity of the substrate HfO₂ nanoparticles toward the acetalization of benzaldehyde is strongly controlled by the transformation of the original ligand head group by the plasma by way of the extent of water adsorption on the surfaces of the pores. These results reinforce the importance of understanding and quantifying the water adsorption on catalytic surfaces to fairly assess the influence of chemistry on catalytic reactivity. 19

RESULTS AND DISCUSSION

HfO₂ nanorods of different ARs were synthesized by heating a solution of hafnium chloride and hafnium isopropoxide in

trioctylphosphine oxide (TOPO) to 340 °C for different times (1, 2, and 4.5 h).²⁰ Ligand exchange was used to replace the original TOPO ligands with oleic acid (OA) ligands on the nanorod surface (cf. Methods in supporting information). Figure 1A-C shows transmission electron microscopy (TEM) micrographs of the OA-capped HfO2 nanorods with three different AR values along with histograms showing the respective diameter and length distributions. While the average diameter of the nanorods is similar at 2.4 ± 0.5 nm, their average lengths are 6.1 \pm 0.3, 12.2 \pm 0.5, and 17.1 \pm 0.9 nm, with AR values of 2.7 ± 0.3 , 4.7 ± 0.4 , and 7.3 ± 0.7 , respectively (the error indicates the 95% confidence interval on the mean value based on a normal distribution, which was not rejected by Kolmogorov-Smirnov or Anderson-Darling tests). For convenience, we label the samples by using the handle "length-ligand-HfO2", for example, 12nm-OA-HfO2 refers to the nanorods with an average length of 12.2 nm and capped with OA.

The nanorods are in the monoclinic phase of HfO_2 . Regardless of the AR value, the X-ray diffraction (XRD) patterns (Figure 1D) show peaks (28.6°, 35.4°, and 50.4°) that are diagnostic of the monoclinic HfO_2 phase, with some evidence of small amounts of tetragonal phase. The (200) peaks of the monoclinic structure (35.4°) become narrower for longer nanorods, consistent with a preferential growth of the nanocrystals along the [100] direction.

Transmission Fourier transform infrared (FT-IR) spectra collected before and after ligand exchange (Figure 1E) indicate that most of the TOPO ligands were replaced by OA. The stretching vibration of P=O (1109 cm⁻¹) decreases significantly after ligand exchange, while the peaks at 1406 and 1548 cm⁻¹ (attributed to the symmetric and asymmetric stretching of COO⁻, respectively)²¹ appear. The relative intensity of the peaks suggests significant deprotonation of OA on the HfO₂ surface. ^{21,22} The broad absorption at 3400 cm⁻¹ in the TOPO-capped HfO₂ nanorods indicates a significant amount of adsorbed water, consistent with our prior findings. ¹⁷

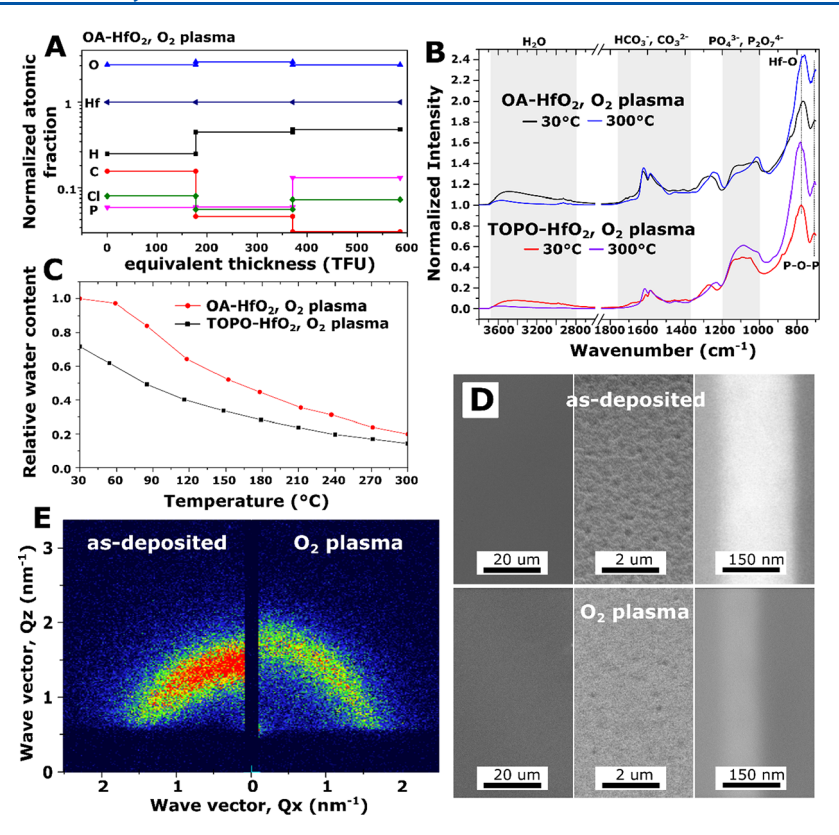


Figure 2. Plasma-processed OA-HfO₂ thin films. (A) Elemental depth profile of 12nm-OA-HfO₂ after O₂ plasma. 0 TFU corresponds to the film surface. The atomic fractions of all elements were normalized to Hf. (B) DRIFTS collected from 12nm-OA-HfO₂ and 14nm-TOPO-HfO₂ samples (~10 mg) under He flow at 30 and 300 °C. The spectra were normalized to the Hf–O phonon vibration peak at 30 °C for both samples, respectively. The shaded areas indicate, from left to right, the peaks attributed to water, bicarbonate/carbonate, and phosphate/pyrophosphates, respectively. (C) Relative water contents in OA- and TOPO-HfO₂ films after O₂ plasma calculated from DRIFTS spectra through area integration between 2600 and 3800 cm⁻¹. (D) SEM micrographs of as-prepared and after O₂ plasma-processed 12nm-OA-HfO₂ thin films (from left to right: low and high magnification of the surface morphology, cross section of the film). (E) GISAXS of thin films for as-prepared and O₂ plasma-processed 12nm-OA-HfO₂.

The particles were then deposited by spin-coating from dispersions in hexane (to produce disordered assemblies of 200-300 nm in thickness)¹⁴ and then processed for 24 h in an inductively coupled plasma (O_2 , 500 mTorr, 30 W).

The plasma processing effectively removes the ligands from the films. The depth profiles of the atomic fractions of each element in the films (plasma-processed OA-HfO₂) were reconstructed from elastic backscattering spectrometry (EBS) and elastic recoil detection (ERD) spectra. For all AR values, the atomic fraction of Hf atoms is constant throughout the film thickness (standard deviation is smaller than 1%), consistent with a lack of concentration gradients (Figure S1). For all values of AR, the carbon fraction (normalized to Hf) is close to 0.1 near the surface, while it decreases to 0.01 inside the film, consistent with the successful removal of ligands by plasma, followed by adventitious contamination after plasma processing (Figure 2A). Residual phosphorus was detected in all films.

While the plasma processing removes the organic fraction of the ligands, the surface chemistry of the ligand-free samples strongly depends on the original ligands. Diffuse reflectance infrared Fourier transform spectra (DRIFTS) collected under He flow show significant differences between plasma-processed 12nm-OA-HfO₂ and 14nm-TOPO-HfO₂ (Figure 2B). Specifically, OA samples show a carbonate-rich surface, whereas TOPO samples show a phosphate-rich surface. Both types of samples show peaks corresponding to pyrophosphates (706

cm⁻¹ and multiple peaks between 1000 and 1200 cm⁻¹)^{25,26} and carbonates (the broad shoulder between 1350 and 1700 cm⁻¹, indicative of multiple binding motifs, e.g., monodentate and bidentate),²⁷ albeit carbonates are significantly more evident in the OA samples. The TOPO samples show a distinct feature at 1090 cm⁻¹ that is consistent with phosphate groups. Pyrophosphates can form during the synthesis of oxide particles with TOPO and are very strongly bound to the oxide surface and resilient to ligand exchange.²⁸

The carbonates likely originate from the adsorption of CO and CO₂ after processing. The phosphates result from oxidation of phosphine oxides in the TOPO samples during plasma processing [X-ray photoelectron spectroscopy (XPS) characterization of the P $2p_{3/2}$ peak is consistent with this explanation, cf. Figure S2]. As the temperature increases, the broad peak at 3400 cm⁻¹ associated with physisorbed water only partially decreases, indicating the presence of a significant amount of strongly bound water, especially in OA-HfO₂ films (Figure 2C). EBS/ERD data are consistent with the presence of strongly bound water: the H/C and O/Hf ratios are inconsistent with adventitious carbon and HfO₂²⁴ but are consistent with adsorbed water in the pores (~6% of the total film volume) (cf. Table S1). 13

Scanning electron microscopy (SEM) characterization of the top surface and cross section of 12nm-OA-HfO₂ thin films before and after 24 h of plasma processing (Figure 2D) shows two key features: the films shrunk significantly (by 54%) in

thickness, but they did not crack in spite of this shrinkage.¹⁴ Samples calcined at 450 °C for 20 h show cracks, holes, and a shrinkage of only 27%, consistent with an incomplete removal of the ligands (Figure S3).^{12,29}

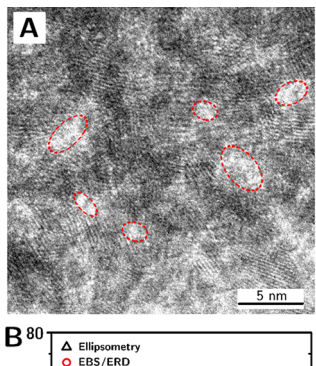
The mechanical properties of the plasma-processed films (cf. Figure S4 and Table S2) were studied with nanoindentation with correction for substrate effects.³⁰ The average film modulus (ranging from 25 to 43 GPa) and hardness (ranging from 1.1 to 1.9 GPa) are compatible with the requirements of CMP steps that are highly common in device manufacturing.³¹

Grazing-incidence small-angle X-ray scattering (GISAXS) shows changes in the arrangement of the nanorods during plasma processing (Figure 2E). The higher intensity for $Q_x = 0$ indicates the existence of order perpendicularly to the substrate before plasma processing, plausibly originating with a preferred orientation of the rods parallel to the substrate. 3Z,33 After plasma processing, the intensity of the scattering is uniform and is stretched to higher Q_z values, indicating a decrease in the interparticle distance perpendicularly to the substrate (consistent with the film shrinkage) and a loss of order (consistent with particle rearrangement resulting from the etching of the ligands).

The plasma-processed films are highly porous. A representative TEM image of 17nm-OA-HfO2 after O2 plasma (Figure 3A) shows pores of 2-3 nm (dashed red circles). The total porosity after plasma processing (Figure 3B) was measured by ellipsometry (black triangles), EBS/ERD (red circles), and Xray reflectometry (XRR, blue squares). While similarly processed films from spherical nanoparticles (~3 nm) had a porosity consistent with a random close-packed array of spheres (\sim 32%), 13,34 the porosity of the nanorod films according to both EBS/ERD and XRR was >50% for all AR values. This porosity is close to the reported porosities of nanocrystal-assembled films using templates $(\sim60\%)^{35,36}$ and much higher than that of nontemplated assemblies (~28%).35,36 Furthermore, these values of porosity are consistent with simulations of random packing of spherocylinders using a mechanical contact method that shows that AR > 2 leads to higher porosities than random close packings of spheres (cf. Figure 3B, purple stars).³⁵

Ellipsometry yielded systematically lower values, plausibly due to the presence of adventitious water, which was not accounted for by the simulation: the difference between the porosities estimated from ellipsometry and EBS/ERD/XRR is consistent with the volume fraction of H_2O ($\sim 6\%$) (cf. Table S1).

Accessible porosity was characterized by EP using toluene as an adsorbate. 38 The adsorption/desorption isotherms from the three different ARs (Figure 3C) show hysteresis of type H2(a), which are unique to mesopores.³⁹ The steep desorption branch indicates pore blocking/percolation or cavitation-induced evaporation because of necks in the pore network.³⁹ The steep desorption branches occur at similar values of relative pressure, indicating that the size of the necks is similar for all ARs. On the other hand, the saturation point of adsorbate uptake scales strongly with the AR (13.3% for 6nm-HfO₂) 19.5% for 12nm-HfO₂, and 21.5% for 17nm-HfO₂) but are smaller than the total porosities. The accessible porosity of 17nm-HfO₂ is close to the reported accessible porosities of nanocrystal-assembled films using templates (20-26% porosities with average pore sizes of 9-17 nm)^{1,40} and higher than the accessible porosity of films made of nanocrystals with similar AR (AR = 7, porosity = 15%). The difference between



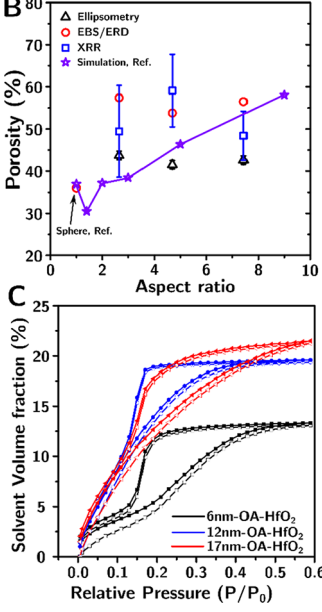


Figure 3. Pore structure of the OA-HfO $_2$ thin film after O $_2$ plasma. (A) TEM micrograph of the 17nm-OA-HfO $_2$ thin films. Some of the pores were marked with red dashed ellipse. (B) Porosity of OA-HfO $_2$ thin films obtained from ellipsometry, EBS, and ERD spectra, and XRR. The simulation result is adapted from ref 37. The porosity of the spherical nanoparticles is adapted from our previous work. (C) Adsorption/desorption hysteresis using toluene as probing molecules measured from EP in an environmental cell. The empty and solid scatters indicate the first and second cycles, respectively.

total and accessible porosity is consistent with (i) the use of a relatively large molecule such as toluene as an adsorbate and (ii) physisorbed water and other adventitious contaminants in the pores (consistent with EBS/ERD analysis). The large dependence of accessible porosity on AR indicates that, while the size of the necks is similar across all ARs, the average size of the pores increases with AR.

The absorption/desorption isotherms are frequently used to calculate pore size distribution using the Barrett–Joyner–Halenda model, which assumes cylindrical pores. The pores in our materials are irregular, so we could only estimate the size of the necks from the steep region of the desorption branch. Two parts compose the pore diameter: the meniscus diameter, $r_{\rm k}$, calculated from the Kelvin equation and the thickness of the adsorbed film, t, calculated from the Brunauer–Emmett–Teller model (cf. Figure S5 and Table S3). The resulting pore neck diameter is 2.7 ± 0.2 nm for all three samples, consistent with the pore sizes observed by TEM.

We estimated the accessible surface area from the isotherms.^{39,44} The nonzero solvent volumes at the starting

pressure of the second cycles suggest that some porosity is irreversibly filled during the first cycle. Therefore, we used the first desorption branch to estimate the specific surface area, which scales with the AR: $91.3~m^2/cm^3$ or $16.8~m^2/g$ for 6nm-HfO2; $126.1~m^2/cm^3$ or $25.5~m^2/g$ for $12nm\text{-HfO}_2$; and $141.9~m^2/cm^3$ or $33.7~m^2/g$ for $17nm\text{-HfO}_2$. These accessible surface areas are comparable to those measured by N_2 adsorption in the ordered mesoporous materials prepared from colloidal Pt nanocrystals through calcination. 1

Controlling pore surface composition is important for applications in catalysis, drug delivery, and sensing.⁴⁵ Plasma-processed TOPO-HfO₂ and OA-HfO₂ samples have significantly different surface chemistries (Figure 4A). We tested the

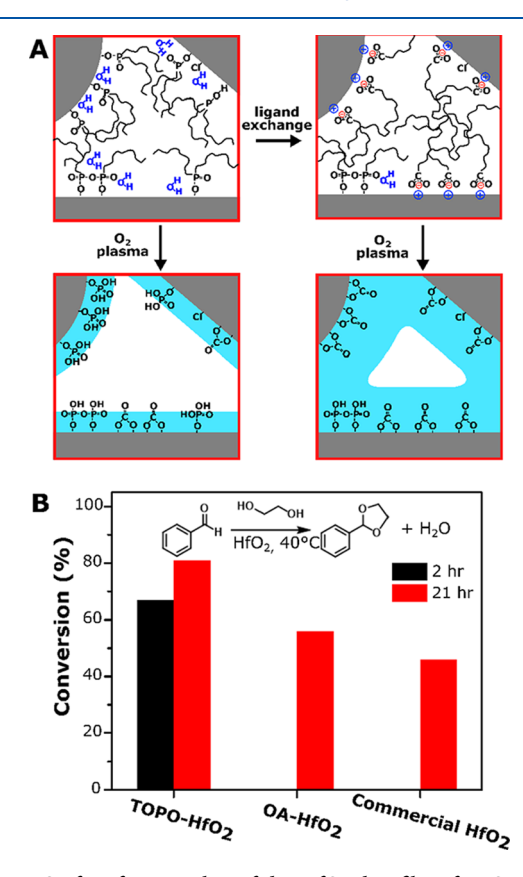


Figure 4. Surface functionality of the HfO_2 thin film after O_2 plasma. (A) Schemes showing the TOPO/OA binding motifs to the surface of HfO_2 nanorods and the surface functional groups left behind after O_2 plasma. The cyan region indicates adsorbed water. (B) Benzaldehyde acetalization catalyzed by HfO_2 prepared from different capping ligands. The conversion of OA- HfO_2 and commercial HfO_2 at 2 h is zero.

effect of these differences on the catalysis of the acetalization of benzaldehyde. The 14nm-TOPO-HfO₂ sample showed high conversion in 2 h, while it took 21 h for the 12nm-OA-HfO₂ sample to achieve similar conversion (Figure 4B). The slower conversion rate on OA-HfO₂ samples may be due to their larger amount of adsorbed water (cf. Figure 2C), which is one of the products for benzaldehyde acetalization and could slow down the diffusion of the reactants to the surface. Furthermore, oxyacid species such as phosphinic and phosphonic acid species are expected to form on the surface of TOPO-HfO₂ nanoparticles during the synthesis²⁸ and could contribute to catalysis of the acetalization reaction. These

species are relatively labile and could be removed upon ligand exchange with OA.

CONCLUSIONS

In summary, we have demonstrated that the plasma processing of films of colloidal nanorods is a practical, rapid, two-step approach to the synthesis of crack-free, all-inorganic, mesoporous films with 100% crystallinity and controlled crystallite size, shape, and surface chemistry. The absence of residual carbon, the nonthermal nature of the processing, and the molecular control over the chemistry of the surfaces make this approach potentially highly desirable for the development of model catalysts for applications or fundamental studies.

ASSOCIATED CONTENT

S Supporting Information

The Supporting Information is available free of charge on the ACS Publications website at DOI: 10.1021/acs.jpcc.9b03723.

Discussions on the tetragonal HfO₂ phase and difference between ellipsometry and XRR analyses; elemental depth profiles in the different kinds of films; XPS of the P 3/2 peak in 14nm-TOPO-HfO₂; SEM of aircalcined 12nm-OA-HfO₂; loading—unloading curves from the nanoindentation experiment; porosity calculation using EBS/ERD; summary of the mechanical properties; calculations of accessible surface area and pore neck diameter; and materials and methods (PDF)

AUTHOR INFORMATION

Corresponding Author

*E-mail: lcademar@iastate.edu.

ORCID 6

Xinchun Tian: 0000-0002-6013-4524 Tian Wei Goh: 0000-0002-4141-3392 Wenyu Huang: 0000-0003-2327-7259

Ludovico Cademartiri: 0000-0001-8805-9434

Author Contributions

X.T. and J.J.C. synthesized the nanoparticles; X.T. cleaned, deposited, and processed the nanoparticles and performed TEM, SEM, FT-IR, and GISAXS characterizations; T.W.G. and W.H. performed catalysis reactions and DRIFTS; O.V. and F.C.P. performed XRR and ellipsometry; J.V. performed adsorption/desorption isotherms; F.N. collected the EBS/ERD data; T.F.d.S. analyzed the EBS/ERD data; J.L.H. performed nanoindentation; B.Y. performed XRD; X.T. and L.C. analyzed the data and wrote the paper.

Notes

The authors declare no competing financial interest.

ACKNOWLEDGMENTS

This work was supported by the Member-Specific-Research-Intel program of Semiconductor Research Corporation under award no. 2015-IN-2582. X.T. is grateful to the Chinese Scholarship Committee for a scholarship. X.T. thanks Prof. Eric W Cochran and Fang-Yi Lin for the help with GISAXS.

REFERENCES

(1) Warren, S. C.; Messina, L. C.; Slaughter, L. S.; Kamperman, M.; Zhou, Q.; Gruner, S. M.; DiSalvo, F. J.; Wiesner, U. Ordered Mesoporous Materials from Metal Nanoparticle–Block Copolymer Self-Assembly. *Science* **2008**, 320, 1748–1752.

- (2) Buonsanti, R.; Pick, T. E.; Krins, N.; Richardson, T. J.; Helms, B. A.; Milliron, D. J. Assembly of Ligand-Stripped Nanocrystals into Precisely Controlled Mesoporous Architectures. *Nano Lett.* **2012**, *12*, 3872–3877.
- (3) Brezesinski, T.; Smarsly, B.; Iimura, K.-i.; Grosso, D.; Boissière, C.; Amenitsch, H.; Antonietti, M.; Sanchez, C. Self-Assembly and Crystallization Behavior of Mesoporous, Crystalline Hfo2 Thin Films: A Model System for the Generation of Mesostructured Transition-Metal Oxides. Small 2005, 1, 889–898.
- (4) Heo, S.; Kim, J.; Ong, G. K.; Milliron, D. J. Template-Free Mesoporous Electrochromic Films on Flexible Substrates from Tungsten Oxide Nanorods. *Nano Lett.* **2017**, *17*, 5756–5761.
- (5) Cargnello, M. Colloidal Nanocrystals as Building Blocks for Well-Defined Heterogeneous Catalysts. *Chem. Mater.* **2019**, 31, 576–596.
- (6) Luo, B.; Xu, S.; Luo, A.; Wang, W.-R.; Wang, S.-L.; Guo, J.; Lin, Y.; Zhao, D.-Y.; Wang, C.-C. Mesoporous Biocompatible and Acid-Degradable Magnetic Colloidal Nanocrystal Clusters with Sustainable Stability and High Hydrophobic Drug Loading Capacity. *ACS Nano* **2011**, *5*, 1428–1435.
- (7) Lu, Z.; Ye, M.; Li, N.; Zhong, W.; Yin, Y. Self-Assembled Tio2 Nanocrystal Clusters for Selective Enrichment of Intact Phosphorylated Proteins. *Angew. Chem., Int. Ed.* **2010**, *49*, 1862–1866.
- (8) Hu, X.; Gong, J.; Zhang, L.; Yu, J. C. Continuous Size Tuning of Monodisperse Zno Colloidal Nanocrystal Clusters by a Microwave-Polyol Process and Their Application for Humidity Sensing. *Adv. Mater.* **2008**, 20, 4845–4850.
- (9) Lu, Z.; Yin, Y. Colloidal Nanoparticle Clusters: Functional Materials by Design. *Chem. Soc. Rev.* **2012**, *41*, 6874–6887.
- (10) Puntes, V. F.; Krishnan, K. M.; Alivisatos, A. P. Colloidal Nanocrystal Shape and Size Control: The Case of Cobalt. *Science* **2001**, *291*, 2115–2117.
- (11) Yin, Y.; Alivisatos, A. P. Colloidal Nanocrystal Synthesis and the Organic–Inorganic Interface. *Nature* **2005**, 437, 664–670.
- (12) Mohapatra, P.; Shaw, S.; Mendivelso-Perez, D.; Bobbitt, J. M.; Silva, T. F.; Naab, F.; Yuan, B.; Tian, X.; Smith, E. A.; Cademartiri, L. Calcination Does Not Remove All Carbon from Colloidal Nanocrystal Assemblies. *Nat. Commun.* **2017**, *8*, 2038.
- (13) Shaw, S.; Silva, T. F.; Bobbitt, J. M.; Naab, F.; Rodrigues, C. L.; Yuan, B.; Chang, J. J.; Tian, X.; Smith, E. A.; Cademartiri, L. Building Materials from Colloidal Nanocrystal Assemblies: Molecular Control of Solid/Solid Interfaces in Nanostructured Tetragonal Zro2. *Chem. Mater.* **2017**, *29*, 7888–7900.
- (14) Shaw, S.; Yuan, B.; Tian, X.; Miller, K. J.; Cote, B. M.; Colaux, J. L.; Migliori, A.; Panthani, M. G.; Cademartiri, L. Building Materials from Colloidal Nanocrystal Arrays: Preventing Crack Formation During Ligand Removal by Controlling Structure and Solvation. *Adv. Mater.* **2016**, *28*, 8892–8899.
- (15) Shaw, S.; Silva, T. F.; Mohapatra, P.; Mendivelso-Perez, D.; Tian, X.; Naab, F.; Rodrigues, C. L.; Smith, E. A.; Cademartiri, L. On the Kinetics of the Removal of Ligands from Films of Colloidal Nanocrystals by Plasmas. *Phys. Chem. Chem. Phys.* **2019**, 21, 1614–1622.
- (16) Shaw, S.; Tian, X.; Silva, T. F.; Bobbitt, J. M.; Naab, F.; Rodrigues, C. L.; Smith, E. A.; Cademartiri, L. Selective Removal of Ligands from Colloidal Nanocrystal Assemblies with Non-Oxidizing He Plasmas. *Chem. Mater.* **2018**, *30*, 5961.
- (17) Shaw, S.; Colaux, J. L.; Hay, J. L.; Peiris, F. C.; Cademartiri, L. Building Materials from Colloidal Nanocrystal Arrays: Evolution of Structure, Composition, and Mechanical Properties Upon the Removal of Ligands by O2 Plasma. *Adv. Mater.* **2016**, *28*, 8900–8905.
- (18) Kendall, K.; McN.Alford, N.; Birchall, J. D. A New Method for Measuring the Surface-Energy of Solids. *Nature* **1987**, 325, 794–796.
- (19) Beichert, P.; Finlayson-Pitts, B. J. Knudsen Cell Studies of the Uptake of Gaseous Hno3 and Other Oxides of Nitrogen on Solid Nacl: The Role of Surface-Adsorbed Water. *J. Phys. Chem.* **1996**, *100*, 15218–15228.
- (20) Depner, S. W.; Cultrara, N. D.; Farley, K. E.; Qin, Y.; Banerjee, S. Ferroelastic Domain Organization and Precursor Control of Size in

- Solution-Grown Hafnium Dioxide Nanorods. ACS Nano 2014, 8, 4678-4688.
- (21) Luo, M.; Olivier, G. K.; Frechette, J. Electrostatic Interactions to Modulate the Reflective Assembly of Nanoparticles at the Oil—Water Interface. *Soft Matter* **2012**, *8*, 11923—11932.
- (22) De Roo, J.; Justo, Y.; De Keukeleere, K.; Van den Broeck, F.; Martins, J. C.; Van Driessche, I.; Hens, Z. Carboxylic-Acid-Passivated Metal Oxide Nanocrystals: Ligand Exchange Characteristics of a New Binding Motif. *Angew. Chem., Int. Ed.* **2015**, *54*, 6488–6491.
- (23) Silva, T. F.; Rodrigues, C. L.; Mayer, M.; Moro, M. V.; Trindade, G. F.; Aguirre, F. R.; Added, N.; Rizzutto, M. A.; Tabacniks, M. H. Multisimnra: A Computational Tool for Self-Consistent Ion Beam Analysis Using Simnra. *Nucl. Instrum. Methods Phys. Res., Sect. B* **2016**, *371*, 86–89.
- (24) Barr, T. L.; Seal, S. Nature of the Use of Adventitious Carbon as a Binding Energy Standard. *J. Vac. Sci. Technol., A* **1995**, *13*, 1239–1246
- (25) Li, Y.; Muto, E.; Aoki, Y.; Kunitake, T. Intermediate-Temperature, Proton-Conducting Membranes of Hafnium Phosphate and Zirconium Phosphate/Borate/Sulfate. *J. Electrochem. Soc.* **2010**, *157*, B1103—B1108.
- (26) Takei, T.; Kobayashi, Y.; Hata, H.; Yonesaki, Y.; Kumada, N.; Kinomura, N.; Mallouk, T. E. Anodic Electrodeposition of Highly Oriented Zirconium Phosphate and Polyaniline-Intercalated Zirconium Phosphate Films. *J. Am. Chem. Soc.* **2006**, *128*, 16634–16640.
- (27) Pokrovski, K.; Jung, K. T.; Bell, A. T. Investigation of Co and Co2 Adsorption on Tetragonal and Monoclinic Zirconia. *Langmuir* **2001**, *17*, 4297–4303.
- (28) De Keukeleere, K.; Coucke, S.; De Canck, E.; Van Der Voort, P.; Delpech, F.; Coppel, Y.; Hens, Z.; Van Driessche, I.; Owen, J. S.; De Roo, J. Stabilization of Colloidal Ti, Zr, and Hf Oxide Nanocrystals by Protonated Tri-N-Octylphosphine Oxide (Topo) and Its Decomposition Products. *Chem. Mater.* **2017**, *29*, 10233–10242.
- (29) Bordia, R. K.; Jagota, A. Crack Growth and Damage in Constrained Sintering Films. J. Am. Ceram. Soc. 1993, 76, 2475–2485.
- (30) Hay, J.; Crawford, B. Measuring Substrate-Independent Modulus of Thin Films. *J. Mater. Res.* **2011**, *26*, 727–738.
- (31) Dubois, G.; Volksen, W.; Magbitang, T.; Miller, R. D.; Gage, D. M.; Dauskardt, R. H. Molecular Network Reinforcement of Sol-Gel Glasses. *Adv. Mater.* **2007**, *19*, 3989–3994.
- (32) Saunders, A. E.; Ghezelbash, A.; Smilgies, D.-M.; Sigman, M. B.; Korgel, B. A. Columnar Self-Assembly of Colloidal Nanodisks. *Nano Lett.* **2006**, *6*, 2959–2963.
- (33) Ye, X.; Chen, J.; Engel, M.; Millan, J. A.; Li, W.; Qi, L.; Xing, G.; Collins, J. E.; Kagan, C. R.; Li, J.; Glotzer, S. C.; Murray, C. B. Competition of Shape and Interaction Patchiness for Self-Assembling Nanoplates. *Nat. Chem.* **2013**, *5*, 466.
- (34) Scott, G. D.; Kilgour, D. M. The Density of Random Close Packing of Spheres. J. Phys. D: Appl. Phys. 1969, 2, 863.
- (35) Vamvasakis, I.; Subrahmanyam, K. S.; Kanatzidis, M. G.; Armatas, G. S. Template-Directed Assembly of Metal—Chalcogenide Nanocrystals into Ordered Mesoporous Networks. *ACS Nano* **2015**, *9*, 4419–4426.
- (36) Brezesinski, T.; Wang, J.; Polleux, J.; Dunn, B.; Tolbert, S. H. Templated Nanocrystal-Based Porous Tio2 Films for Next-Generation Electrochemical Capacitors. *J. Am. Chem. Soc.* **2009**, *131*, 1802–1809.
- (37) Williams, S. R.; Philipse, A. P. Random Packings of Spheres and Spherocylinders Simulated by Mechanical Contraction. *Phys. Rev. E: Stat., Nonlinear, Soft Matter Phys.* **2003**, *67*, 051301.
- (38) Baklanov, M. R.; Mogilnikov, K. P.; Polovinkin, V. G.; Dultsev, F. N. Determination of Pore Size Distribution in Thin Films by Ellipsometric Porosimetry. *J. Vac. Sci. Technol., B: Microelectron. Nanometer Struct.*—Process., Meas., Phenom. 2000, 18, 1385—1391.
- (39) Thommes, M.; Kaneko, K.; Neimark, A. V.; Olivier, J. P.; Rodriguez-Reinoso, F.; Rouquerol, J.; Sing, K. S. W. Physisorption of Gases, with Special Reference to the Evaluation of Surface Area and

Pore Size Distribution (Iupac Technical Report). *Pure Appl. Chem.* **2015**, *87*, 1051–1069.

- (40) Ondry, J. C.; Robbennolt, S.; Kang, H.; Yan, Y.; Tolbert, S. H. A Room-Temperature, Solution Phase Method for the Synthesis of Mesoporous Metal Chalcogenide Nanocrystal-Based Thin Films with Precisely Controlled Grain Sizes. *Chem. Mater.* **2016**, *28*, 6105–6117.
- (41) Barrett, E. P.; Joyner, L. G.; Halenda, P. P. The Determination of Pore Volume and Area Distributions in Porous Substances. I. Computations from Nitrogen Isotherms. *J. Am. Chem. Soc.* **1951**, 73, 373–380.
- (42) Gregg, S.; Sing, K. Adsorption, Surface Area and Porosity; Academic Press Inc. (London) Ltd, 1982.
- (43) Boissiere, C.; Grosso, D.; Lepoutre, S.; Nicole, L.; Bruneau, A. B.; Sanchez, C. Porosity and Mechanical Properties of Mesoporous Thin Films Assessed by Environmental Ellipsometric Porosimetry. *Langmuir* **2005**, *21*, 12362–12371.
- (44) Emmett, P. H.; Brunauer, S. The Use of Low Temperature Van Der Waals Adsorption Isotherms in Determining the Surface Area of Iron Synthetic Ammonia Catalysts. *J. Am. Chem. Soc.* **1937**, *59*, 1553–1564.
- (45) Brühwiler, D. Postsynthetic Functionalization of Mesoporous Silica. *Nanoscale* **2010**, *2*, 887–892.